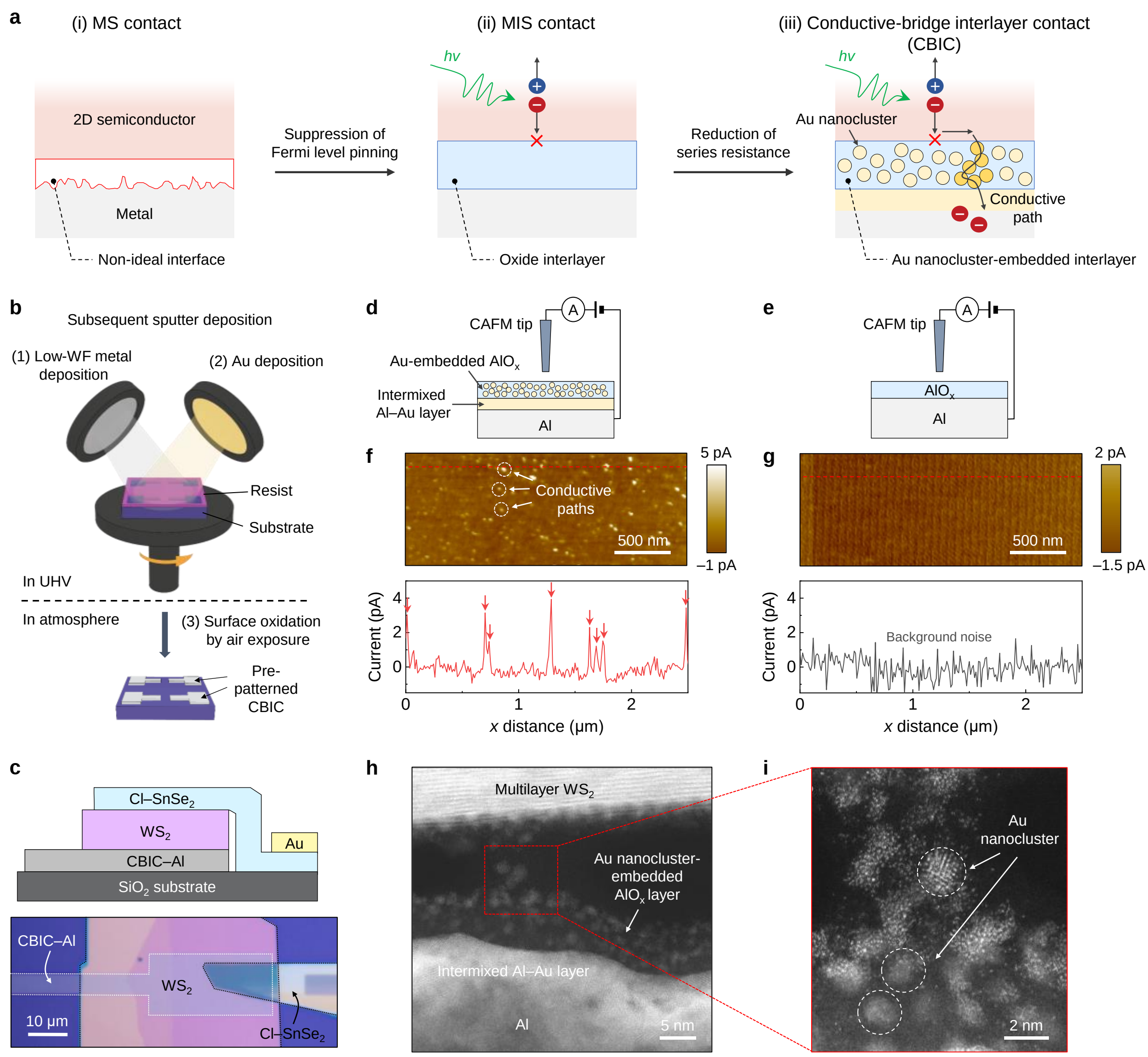

Fig. 1 | Concept of the conductive-bridge interlayer contact. a, Comparison of the proposed and traditional contact architectures: (i) metal–semiconductor (MS) contact; (ii) metal–interlayer–semiconductor (MIS) contact; (iii) conductive-bridge interlayer contact (CBIC). Efficient carrier extraction can occur through conductive pathways in the CBIC, a feature absent in conventional MIS contacts. **b,** Schematic of the CBIC fabrication process via sequential sputter deposition. **c,** Schematic (upper) and optical image (lower) of a complete device, where a WS_2 absorber is sandwiched between CBIC–Al and Cl–$SnSe_2$ electrodes. **d,e,** Schematics of conductive atomic force microscopy (CAFM) measurements on CBIC–Al with Au (**d**) and without Au (**e**). **f,g,** Corresponding CAFM current maps (upper) and current line profiles (lower) of **d** and **e**, respectively. Conductive pathways are denoted by white arrows. The current line profile data are taken along the dashed red lines. **h,** Cross-sectional STEM image of the contact between WS_2 and CBIC–Al. Note that the bright spots near the bottom WS_2 layer might be residual interlayer particles after focused ion beam milling. **i,** Enlarged STEM image of the selected area in **h**, clearly revealing a uniform distribution of Au nanoclusters within the AlO_x interlayer.

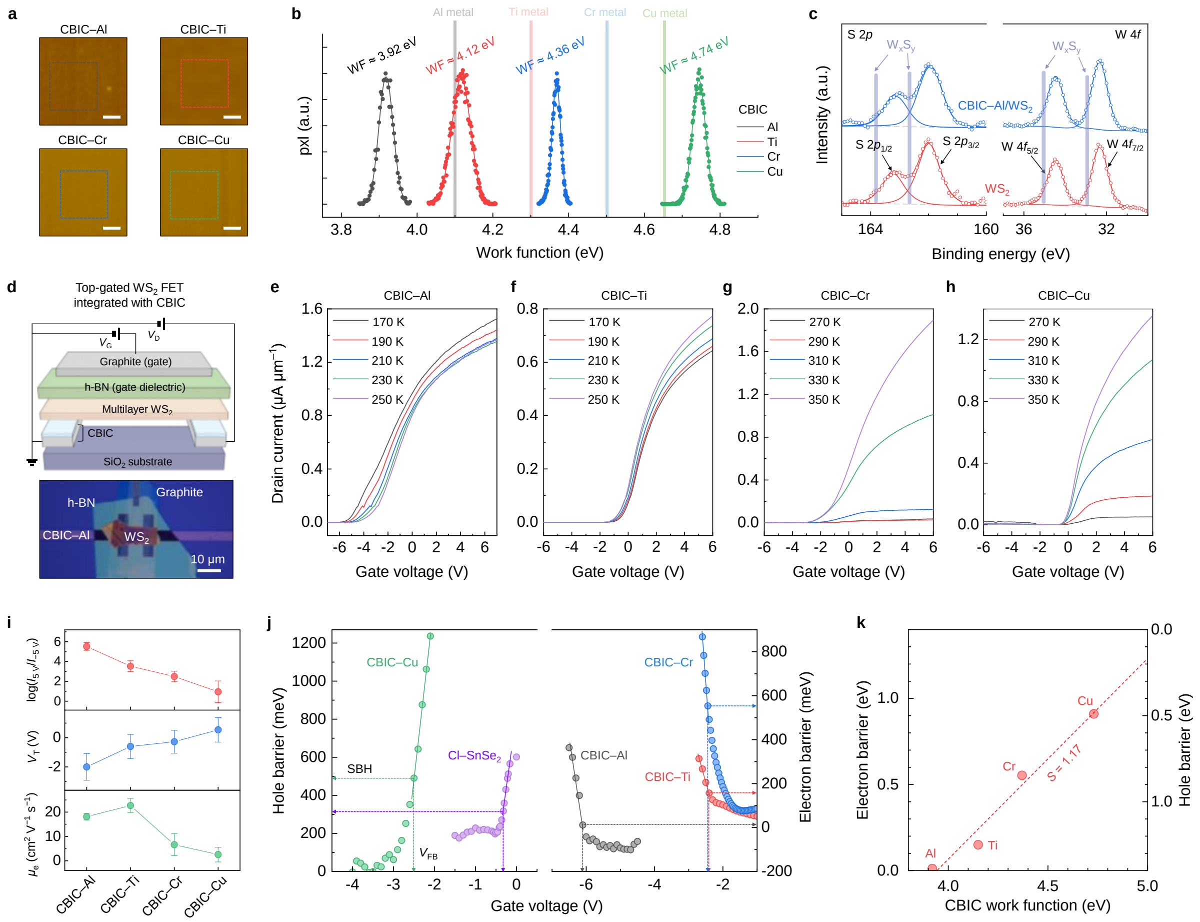

Fig. 2 | Characterization of the CBIC. a, Kelvin probe force microscopy images of various CBICs. Scale bars, 1 μm. **b,** Work function (WF) distributions of the CBIC acquired from the indicated areas in **a**. The shaded stripes indicate the WFs of pristine metals taken from literature[8,19]. **c,** X-ray photoelectron spectroscopy spectra of WS_2 before and after CBIC–Al integration. **d,** Schematic (upper) and optical image (lower) of a top-gated WS_2 transistors fabricated with CBICs. **e–h,** Temperature-dependent transfer curves of WS_2 devices with CBIC–Al (**e**), Ti (**f**), Cr (**g**), and Cu (**h**) at $V_{DS} = 1$ V. **i,** Carrier polarity, threshold voltage (V_T), and electron field-effect mobility (μ_e) for different CBICs. The error bars represent the standard deviation for at least six samples in each case. **j,** Effective barrier height of each contact as a function of gate voltage. The Schottky barrier height is estimated under the flat band voltage condition ($V_{GS} = V_{FB}$), which corresponds to the onset of deviation from the linear trend. **k,** Estimated Schottky barrier heights for different contacts. The S value of the CBIC was extracted from linear fitting, denoted by the red dashed line.

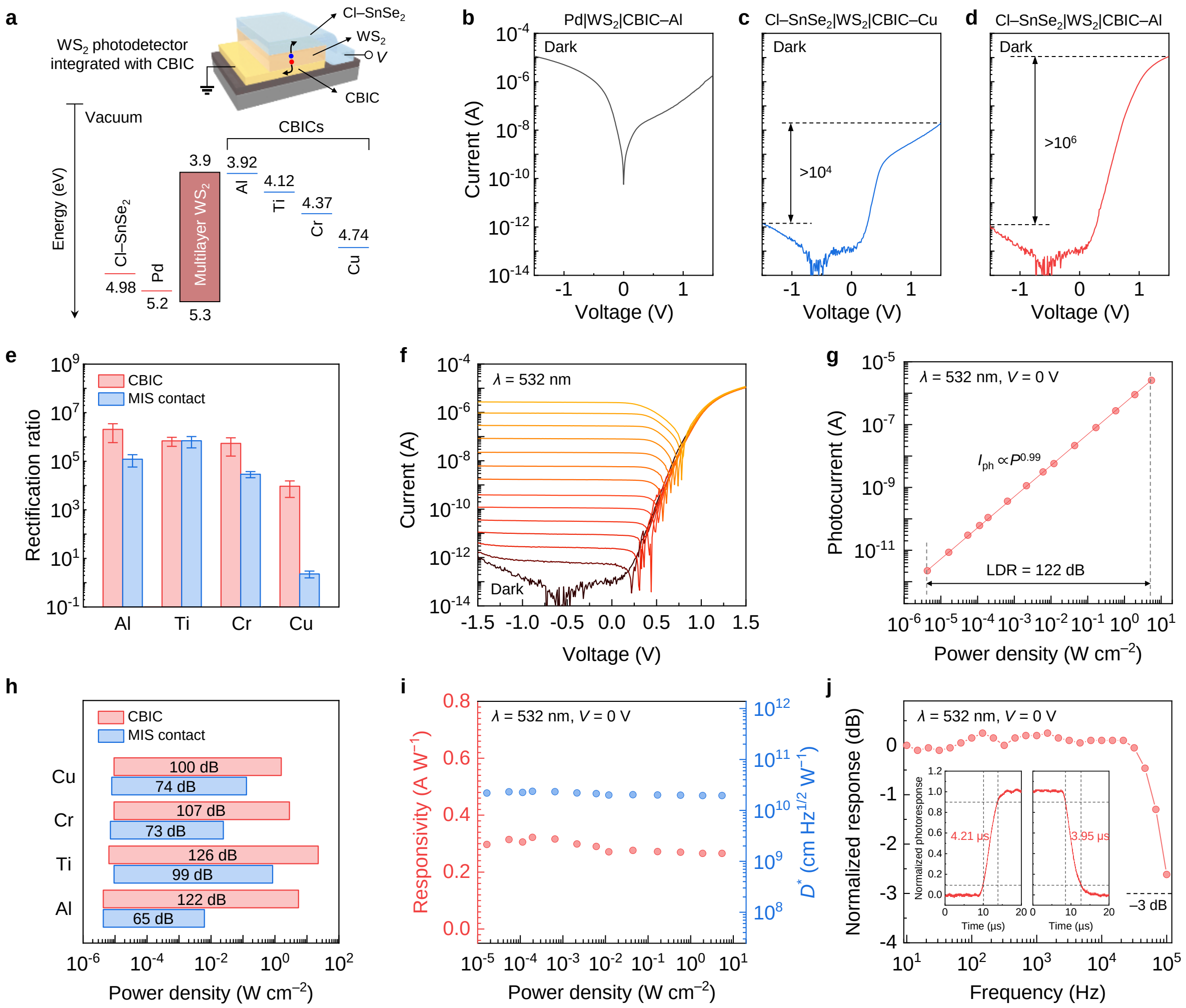

Fig. 3 | Characteristics of the CBIC-integrated 2D photodetector. a, Schematic of the CBIC-integrated 2D WS_2 photodetector (upper) and energy level diagram (lower) of the materials used in this study. **b–d,** *I*–*V* characteristics of diodes for different contact configurations. **e,** Current rectification ratio between $I_{1.5V}$ (I_{DS} at $V = 1.5$ V) and $I_{-1.5V}$ (I_{DS} at $V = -1.5$ V) for different contacts. Error bars represent the standard deviation for seven samples in each case. **f,** *I*–*V* curves of the representative CBIC–Al device measured under 532 nm laser illumination with power densities varying from 4.3 μW cm^{-2} to 5.4 W cm^{-2}. **g,** Short-circuit ($V = 0$ V) photocurrent as a function of light power density. The estimated linear dynamic range (LDR) of the device is over 120 dB. **h,** Comparison of the LDR of devices with different contacts. The CBIC devices generally exhibit a higher LDR compared to MIS devices. **i,** Responsivity and specific detectivity as a function of light power density. **j,** Normalized photoresponse as a function of modulated frequency, showing a −3 dB cutoff frequency exceeding 100 kHz. Insets: Plots of time-resolved photoresponse showing estimated rise and fall times of 4.21 μs and 3.95 μs, respectively.

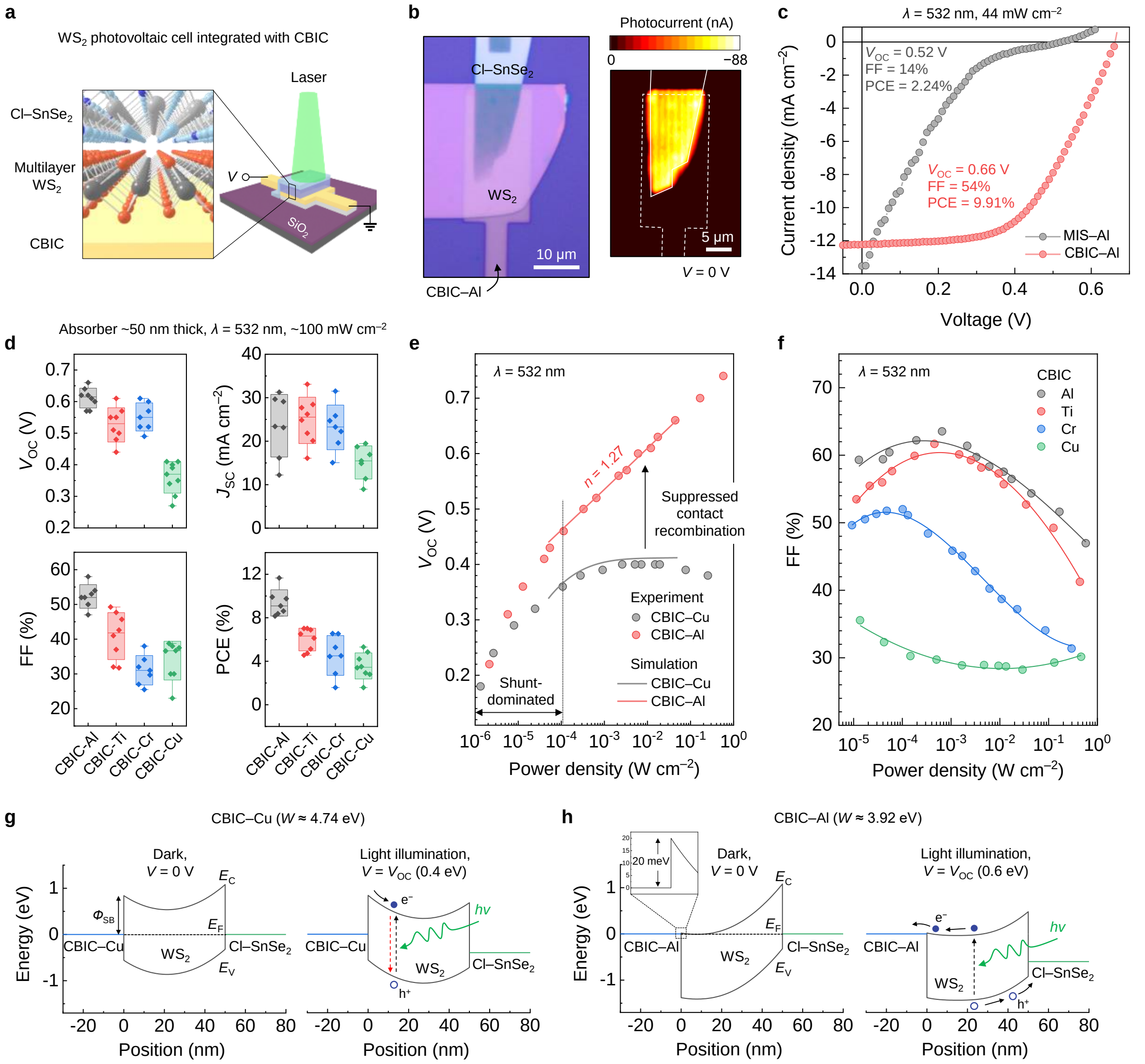

Fig. 4 | Characteristics of the CBIC-integrated 2D photovoltaic cell. a, Schematic of the CBIC-integrated 2D WS_2 photovoltaic cell. **b,** Optical image (left) and corresponding photocurrent map (at $V = 0$ V) of the device. CBIC–Al and Cl–$SnSe_2$ electrodes are indicated by dashed and solid lines, respectively. **c,** J–V curves of the CBIC–Al and MIS–Al devices, measured under light illumination (532 nm, 44 mW cm^{-2}). **d,** Photovoltaic parameters of devices with different CBICs. Each data point corresponds to an individual device. Statistical distribution is represented in box-and-whisker plots (line within box: median, box limit: standard deviation, whiskers: 1.5 outliers). **e,** Plot of V_{OC} as a function of light intensity. Use of CBIC–Al can mitigate contact recombination and facilitate electron extraction, achieving a high V_{OC}. **f,** Plot of FF as a function of light intensity. **g,h,** Simulated band diagrams of the devices with CBIC–Cu (**g**) and CBIC–Al (**h**) under dark and light illumination conditions. The red dashed arrow in **g** indicates the contact recombination of electrons and holes. Inset: Enlarged view of the black dashed rectangle showing a negligible electron barrier of 20 meV.

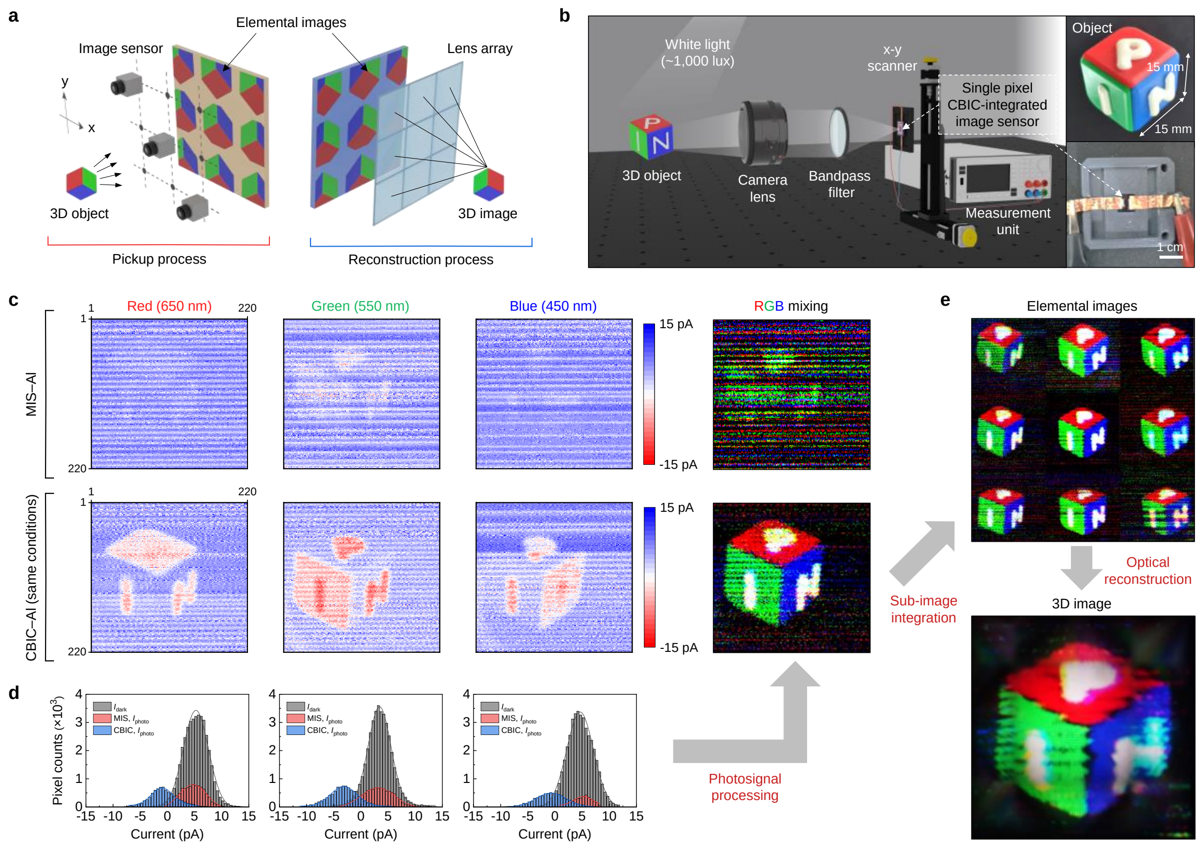

Fig. 5 | Full-colour 3D imaging using CBIC-integrated image sensors. a, Principle of the 3D integral imaging method. **b,** Schematic and photographs of the 3D imaging system using a CBIC–Al device as a single-pixel imager. **c,** Spatial photocurrent images for various wavelengths (650 nm, 550 nm, and 450 nm, left) and corresponding full-colour images (right), acquired from MIS–Al (top) and CBIC–Al (bottom) devices. **d,** Photocurrent distributions of the MIS–Al and CBIC–Al devices for different wavelengths: 650 nm (left), 550 nm (middle), and 450 nm (right). Gaussian fittings are indicated by the solid lines. **e,** Full-colour elemental image (top) and the optically reconstructed 3D image (bottom), clearly depicting the 3D object with white letters *P*, *I*, and *N*. Details on the reconstruction process are provided in Supplementary Video 1.